High-Throughput Characterization of Transition Metal Dichalcogenide Alloys: Thermodynamic Stability and Electronic Band Alignment

Citation for the original published paper (version of record):
Linderälv, C., Rahm, M., Erhart, P. (2022). High-Throughput Characterization of Transition Metal Dichalcogenide Alloys: Thermodynamic
Stability and Electronic Band Alignment. Chemistry of Materials, 34: 9364-9372.
http://dx.doi.org/10.1021/acs.chemmater.2c01176

CHEMISTRY OF MATERIALS

pubs.acs.org/cm

Article

High-Throughput Characterization of Transition Metal Dichalcogenide Alloys: Thermodynamic Stability and Electronic Band Alignment

Christopher Linderälv, J. Magnus Rahm, and Paul Erhart*

Cite This: https://doi.org/10.1021/acs.chemmater.2c01176

Read Online

ACCESS | Metrics & More | Article Recommendations | Supporting Information

ABSTRACT: Alloying offers a way to tune many of the properties of the transition metal dichalcogenide (TMD) monolayers. While these systems in many cases have been thoroughly investigated previously, the fundamental understanding of critical temperatures, phase diagrams, and band edge alignment is still incomplete. Based on first-principles calculations and alloy cluster expansions, we compute the phase diagrams of 72 TMD monolayer alloys and classify the mixing behavior. We show that ordered phases in general are absent at room temperature but that there exist some alloys that have a stable Janus phase at room temperature. Furthermore, for a subset of these alloys, we quantify the band edge bowing and show that the band edge positions for the mixing alloys can be continuously tuned in the range set by the boundary phases.

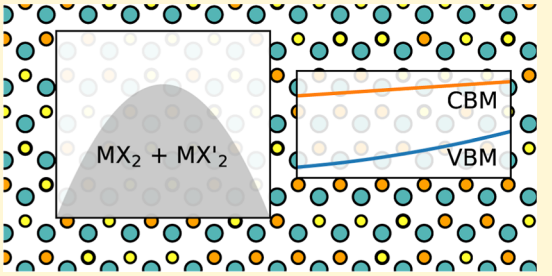

1. INTRODUCTION

Monolayer transition metal dichalcogenides (TMDs) constitute a class of two-dimensional (2D) materials, commonly of MX_2 stoichiometry, where M is a transition metal (e.g., Mo, W, Zr, Hf, Ti, Pd, and Pt) and X is a chalcogen (S, Se, and Te). These monolayer compounds exhibit a structure where the transition metal is sandwiched between chalcogen atoms and exhibit hexagonal or trigonal symmetry (Figure 1a). TMDs have received a considerable amount of attention over the last decade, for example, due to the excellent optical properties of the semiconducting group VI TMD MoS_2,[1] the prospects of vertical integration into heterostructures,[2] the emergent properties of moiré structures,[3,4] and the outlook of using TMDs as catalysts for the hydrogen evolution reaction.[5] Many TMD monolayers exhibit moderate band gaps of around 1−3 eV, which is suitable for photochemical applications or for use as channel materials in nanoelectronics.[6−8] Due to the emergence of high-κ dielectrics as gate material in transistors such as ZrO_2 and HfO_2, (2D) TMDs based on the same transition metals may also play a role in future high-κ transistor designs.[9]

The electrical transport properties as well as the optical response are ultimately dependent on band edge positions. The position of the band edges are particularly important in devices based on heterojunctions. Specifically, TMD heterostructures with type-II alignment can be used for photoseparation of charge carriers.[10] There are various ways to tailor the electronic properties, including functionalization,[11] Coulomb engineering,[12−14] strain engineering,[15,16] and alloying.[14,17,18] While alloying may allow for a continuous tuning of the band edge position, not all alloys can be manufactured due to their inherent thermodynamical properties. The main objectives of this work are therefore to map out the phase diagrams of a large number of binary TMD alloys and the band edge variations of promising alloy combinations.

All of the binary alloys based on (Mo,W) $(S,Se)_2$ have been synthesized,[19] usually in the hexagonal H structure (space group $P\bar{6}m2$, ITCA number 187; Figure 1b), and have been thoroughly studied in the context of band gap engineering by composition control.[18,20−25] It has been shown that these alloys are random at ambient conditions due to (very) small mixing energies.[18] Although ordered phases have been found in computational studies,[19] these are not observed in experiments,[26,27] most likely due to the very small energy gains on the order of 1 meV compared to that of the respective disordered solution. In addition, the $MoS_{2x}Te_{2(1-x)}$ alloy has been fabricated.[28] For the optical properties, in particular, it is relevant whether alloying preserves the valley degree of freedom found in the boundary phases, that is, the non-alloyed systems. In this regard, it is noteworthy that, for example, $Mo_xW_{1-x}S_2$ has been recently shown to be robust in this regard.[27]

While the group VI TMD alloys have been extensively studied, the prospect of alloying these TMDs with transition metals from other groups of the periodic table has not been

Received: April 19, 2022
Revised: September 27, 2022

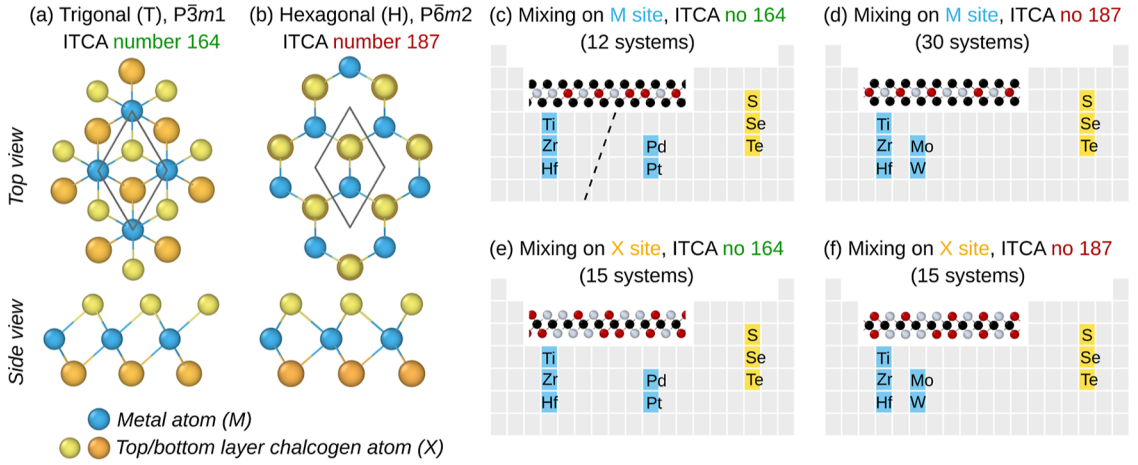

Figure 1. Overview of the 72 TMD monolayer alloys considered in this work in (a) space group $P\bar{3}m1$ (ITCA number 164) and (b) space group $P\bar{6}m2$ (ITCA number 187). The alloys consisted of either (c,d) two species on the metal (M) site and one (no alloying) on the chalcogen (X) site or (e,f) one species (no alloying) on the M site and two species on the X site. For space group 164, we considered Ti, Zr, Hf, Pd, and Pt on the M site, but we never mixed Ti/Zr/Hf with Pd/Pt. For space group 187, we considered Ti, Zr, Hf, Mo, and W. The X site was always occupied by S, Se, or Te, either just one of them (M-site mixing) or a mixture of two of them (X-site mixing).

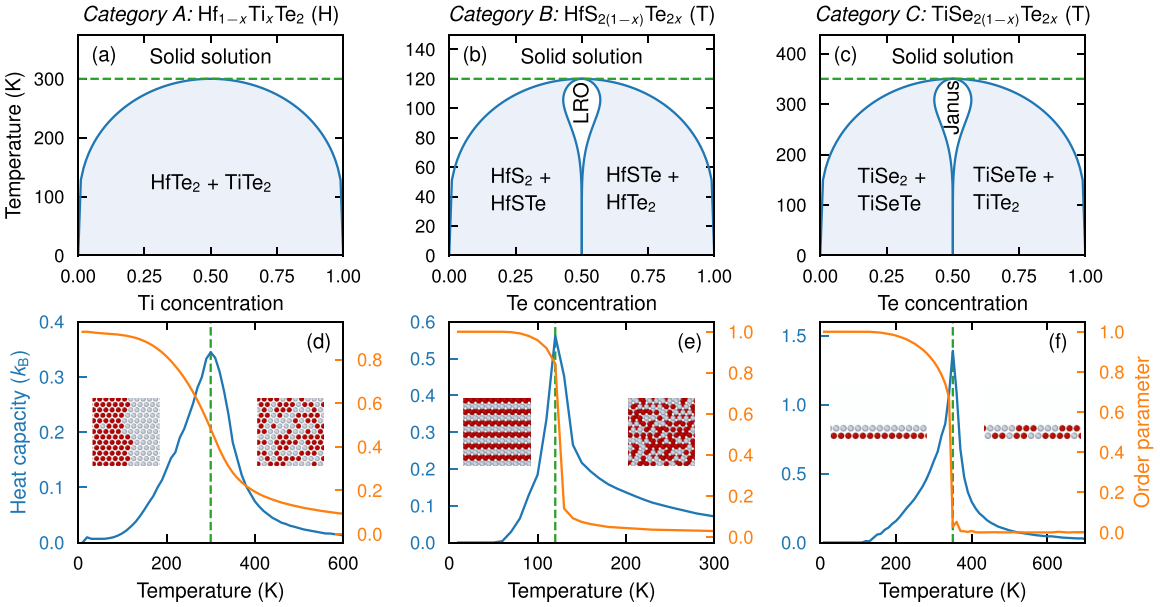

Figure 2. Schematic phase diagrams of systems that show (a) phase separation (category A), (b) intermediate phase at 50% with a long-range in-plane order (category B) and (c) intermediate phase at 50% with a long-range out-of-plane (or Janus-type) order (category C). (d–f) The critical temperatures (dotted, green lines) are identified as the position of the peak in heat capacity (blue lines), as calculated with MC simulations at 50% concentration. The peaks correspond to a rapid decline in the relevant order parameter (orange lines), here chosen as the (d) first-nearest neighbor short-range order, (e) in-plane structure factor, and (f) difference in concentration between the two layers (for details, see Supporting Information Note S3). Insets show snapshots of small parts of the structures in the MC simulations [top view in (d,e) and side view in (f)].

systematically addressed, although doping of, for example, MoS_2 with Ti has been reported.[29] In addition, there are various families of TMDs, including different structural prototypes, for which the alloying behavior is largely unexplored. The TMD monolayers based on Zr, Hf, Pd, and Pt preferentially crystallize in the trigonal T phase (space group $P\bar{3}m1$, ITCA number 164; Figure 1a)[30−33] and exhibit indirect band gaps. The basic electronic structure and excitation spectra of Zr- and Hf-based boundary phase TMDs have been studied previously.[34] Some theoretical[35] and experimental[36,37] studies on the electronic properties of the layered bulk alloys exist, but to the best of our knowledge, the thermodynamic and electronic properties of T-TMD monolayer alloys have not been systematically addressed.

A special subclass of monolayer alloys are Janus monolayers, that is, ordered MXX′ compounds where the chalcogens X and X′ occupy the top and bottom layer sides of the TMD sheet. Janus monolayers have been suggested to be useful for band alignment engineering[14] and as catalysts for the hydrogen evolution reaction.[38] Furthermore, theoretical studies have suggested that several materials may exhibit Janus phases.[39] While some Janus structures have been manufactured,[40] little is known about the general thermodynamical stability of these phases.

https://doi.org/10.1021/acs.chemmater.2c01176
Chem. Mater. XXXX, XXX, XXX−XXX

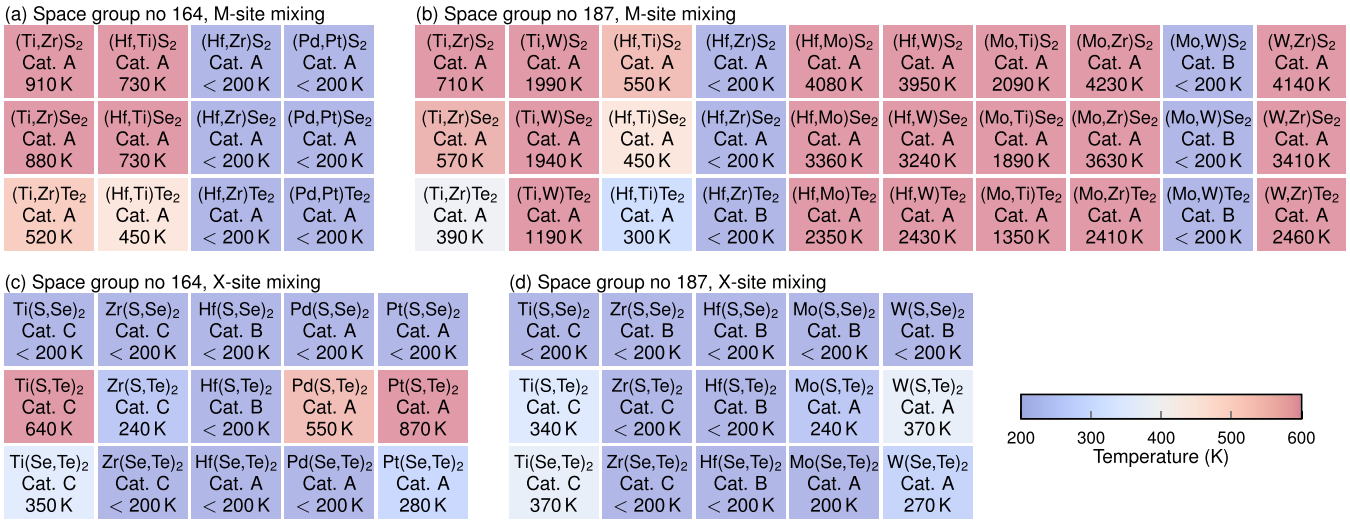

Figure 3. Mixing behavior and critical temperatures for all 72 systems studied here. Each box indicates the predicted mixing behavior close to zero temperature: *category A* for non-mixing systems that phase separate (lateral heterostructures), *category B* for systems that form alloys with long-range order, and *category C* for systems that form Janus monolayers. Temperatures indicate the predicted critical temperatures (rounded to nearest 10 K) at which this quality is lost at 50% concentration. Colors are proportional to the critical temperatures.

In this work, we aim to provide a more comprehensive perspective of TMD monolayer alloys. We consider 72 binary alloys of the T and H structure types (Figure 1) and focus on their thermodynamic properties, specifically the underlying phase diagrams, and electronic properties, specifically band edge positions (for the semiconducting systems) and work functions (for the metallic systems). In the next section, we outline the methodology used in this work with details provided in the Supporting Information. This is followed by a description and discussion of the phase diagrams and mixing characteristics in Section 3.1. Models for the critical temperature and the structural categorization are presented in Section 3.2, while the computed band edge positions and bowing parameters are summarized in Section 3.3.

2. METHODOLOGY

Here, we study the thermodynamic and electronic properties of TMD alloys with chemical formula MX_2 (Figure 1) in the T structure (space group $P\bar{3}m1$, ITCA number 164) and the H structure (space group $P\bar{6}m2$; ITCA number 187). For the T structure, we consider mixing on the M-site involving Ti, Zr, and Hf (nine systems) and Pd and Pt (three systems) as well as X-site mixing (15 systems). For the H structure, we consider mixing on the M-site, involving Ti, Zr, Hf, Mo, and W (30 systems), as well as X-site mixing (15 systems). These alloys were selected based on the known stability or metastability of the boundary phases, as documented in the Computational 2D Materials Database.[32]

To assess the thermodynamic properties of these TMD alloys, we constructed alloy cluster expansions[41,42] (Supporting Information Note S2) using reference data from density functional theory (DFT) calculations[41,43−49] (Supporting Information Note S1). These models were subsequently sampled using Monte Carlo (MC) simulations[41,50] to obtain phase diagrams and critical temperatures (Supporting Information Note S3).

We then carried out a further characterization of the electronic properties of these systems, specifically focusing on the band gap and the position of the conduction and valence band edges using DFT calculations and special quasi-random structures (SQSs) to mimic complete (fully random) mixing[41,43−47,51−55] (Supporting Information Note S4). From the latter analysis, we excluded alloy systems with very high critical temperatures, leaving us with 21 and 27 systems in structure types T and H, respectively.

3. RESULTS AND DISCUSSION

3.1. Thermodynamic Properties. The mixing behavior at zero temperature can be grouped into three different categories: (A) systems that exhibit two boundary phases separated by a miscibility gap and no long-range ordered mixed phase (Figure 2a) as well as systems that exhibit a long-range ordered phase at 50% composition with (B) in-plane order (Figure 2b) or (C) out-of-plane order (Figure 2c), a situation that is commonly referred as a Janus system.[40] The critical temperatures are evaluated by the peak in heat capacity, as calculated using MC simulations at 50% concentration. The peaks correspond to a rapid decline in the relevant order parameter, see Figure 2d−f.

Out of the 72 alloys considered, we find that 49 alloys fall into category A (Section 3.1.1), 12 into category B (Section 3.1.2), and 11 into category C (Section 3.1.3). These categories are discussed in more detail in the following sections.

3.1.1. Category A: Phase Separation into Boundary Phases. 3.1.1.1. M-Site Mixing with Elements from Different Groups. Among the 38 M-site alloys that are non-mixing at zero temperature, 18 have critical temperatures above approximately 1200 K (Figure 3a,b), which suggests that these combinations should be difficult to stabilize, if at all. This group comprises all alloys that mix species from different groups of the periodic table on the M-site such as Hf and Mo or W and Zr. According to the Hume-Rothery rules, well-established for the metallic alloys,[56] this behavior can be rationalized by the electronegativity differences. The group IV elements exhibit electronegativities of 1.3−1.5 on the Pauling scale,[57] whereas the group VI transition metals have values from 2.2 to 2.4 (Table S4). This indicates that the bonding in TMDs involving group IV species is much more ionic than in their counterparts from group VI. For some of these alloying

https://doi.org/10.1021/acs.chemmater.2c01176
Chem. Mater. XXXX, XXX, XXX−XXX

systems, for example, Zr_xMo_{1-x2} and $Ti_xMo_{1-x}Te_2$, there is even a sign difference in the Born effective charges (BECs) (Table S3), which is a further indication of the incompatibility of the mixing species. The critical temperature of alloys involving combinations of Zr or Hf with Mo or W is only weakly dependent on the specific transition metal combination. Rather, the critical temperature is primarily determined by the chalcogen species, with S- and Te-containing systems exhibiting the highest and lowest critical temperatures, respectively.

3.1.1.2. M-Site Mixing with Elements from the Same Group. The remaining 20 non-mixing M-site alloys have critical temperatures below approximately 900 K (Figure 3a,b). The nine systems that do not contain Ti even have critical temperatures below 200 K and should thus be readily miscible. The smaller miscibility in Ti-containing systems can be explained by the much larger difference in the lattice parameter between Ti- and Zr/Hf-based TMDs (Table S3), which is mirrored by the electronegativity differences (Table S4). In fact, as is discussed in Section 3.2, the lattice parameters of the boundary phases are in general strong predictors for miscibility. As in the case of M-site mixing with elements from different groups, the critical temperatures decrease monotonically from S via Se to Te.

3.1.1.3. X-Site Mixing. The critical temperatures for non-mixing X-site alloys are generally very low, with the sole exception of the $MS_{2x}Te_{2(1-x)}$ alloys with Pd and Pt that still exhibit values of 550 and 870 K, respectively (Figure 3c,d). Generally, the highest critical temperatures are obtained for S−Te alloys, which can be attributed to the large lattice mismatch between the MS_2 and MTe_2 boundary phases. We note that according to the Hume-Rothery rules, a 15% difference or more in the covalent radii should indicate immiscibility. Nevertheless, for the present systems, the covalent radius is not a good predictor for how well Te mixes with other chalcogen species. This is confirmed by the analysis in Section 3.2.

3.1.2. Category B: Systems with In-Plane Ordering. The systems in this category include both M-site and X-site mixing that all exhibit an intermediate phase at 50% with in-plane ordering (Figure 2b).

There are four M-site alloys, namely, H-$Mo_xW_{1-x}X_2$ with X = S, Se, and Te as well as H-$Hf_xZr_{1-x}Te_2$ (Figure 3b), and eight X-site alloys, including H-$MS_{2x}Se_{2(1-x)}$ with M = Mo, W, and Zr as well as five Hf-based systems (Figure 3c,d). The only X-site Hf-based alloy that does not exhibit this type of long-range order is T-$HfSe_{2x}Te_{2(1-x)}$.

Generally, the ordering tendency is weak and the critical temperatures are all below 200 K. For almost all practical purposes, these systems can be therefore considered as fully miscible.

3.1.3. Category C: Systems with Out-of-Plane (Janus-Type) Ordering. The systems in this category have the general composition MXX′ where one chalcogen species (X) occupies the lattice sites above the transition metal and the other chalcogen species (X′) occupies the sites below.

All Ti- and Zr-based X-site alloys in both T and H structure types with the single exception of H-ZrSSe have a Janus ground state at 50% composition. The critical (order−disorder) temperature was obtained from MC simulations by following the difference in the composition in each individual layer. The thus obtained critical temperatures are above room temperature for T-TiSTe, T-TiSeTe, H-TiSTe, and H-TiSeTe with a value as high as 640 K for TiSTe, indicating remarkable stability. To the best of our knowledge, these Janus monolayers have not been synthesized yet. On the other hand, we find MoSSe, which has in fact been synthesized,[40] to be *thermodynamically* unstable in the present study (Figure S6). While the Janus monolayer is in fact the isomolar alloy with the highest energy, its energy is only about 13 meV/site equivalent to about 150 K, and thus, the driving force for decomposing such a structure is very small. This supports the notion that the growth conditions play a crucial role in enabling the formation of these structures.

It is instructive to consider the factors that lead to thermodynamically stable Janus monolayers by comparing the prototypical cases of H-MoSSe and T-ZrSSe. The basic parameters of the boundary systems in these two cases are very similar (Table S3). The most striking difference is the observed BECs, which differ qualitatively. While in H-MoSSe, the elements of the BEC tensor are negative, as has been shown for the boundary phases also in other studies,[58] in T-ZrSSe, these elements are positive. This finding is supported in Section 3.2, where we construct a classifier for phase behavior, which reveals that the BECs are important indicators for the appearance of thermodynamically favorable Janus structures.

3.1.4. Comparison with the Experiment. Experimentally, very little data are available with regard to the thermodynamic properties of TMD alloys, which can be attributed to the considerable difficulties associated with such measurements. It has been observed that phase separation in $MoS_{2x}Te_{2(1-x)}$ occurs mainly on the Te-rich side,[59] which was suggested to be due to the formation of the distorted 1T′ phase. In the present study, we have only considered isostructural phase diagrams, but nonetheless, we observe an asymmetric binodal (Figure S6). At 80% S, the alloy should phase-separate at around 275 K, whereas for 20%, this temperature increases to around 325 K. This suggests that the experimentally observed asymmetry could be already be explained by the thermodynamics of the isostructural system.

For the $Mo_{1-x}W_xS_2$ alloy, random mixing at room temperature for crystals grown with chemical vapor transport was recently shown,[27] which is what is expected from the present determination of the critical temperature for the order−disorder transition of 30 K.

The present study also has potential implications for the understanding of the formation and stability of 2D lateral heterostructures. It is apparent that the existence of a miscibility gap is not a prerequisite for forming lateral heterostructures with sharp interfaces. Such a configuration has, for example, been realized between MoS_2 and WS_2,[60,61] for which both the present and earlier calculations predict a clear preference for mixing (Figure S5). The small negative mixing energy of down to −6.5 meV/site in combination with the mixing entropy should imply that such interfaces roughen and vanish at sufficient temperatures when sufficient kinetic activation enables the system to achieve a thermodynamically more favorable configuration.

On the other hand, for phase-separating systems, which can be synthesized in the mixed form under non-equilibrium growth conditions, high-temperature annealing may be used to construct temperature stable lateral heterostructures.[62] In this context, Figures 3 and 6 provide guidance as to which heterostructures can and cannot be manufactured using annealing. For example, the proposed lateral heterostructure of T-ZrS_2 and T-HfS_2[63] is likely to require synthesis techniques

https://doi.org/10.1021/acs.chemmater.2c01176
Chem. Mater. XXXX, XXX, XXX−XXX

beyond thermal annealing due to the low critical temperature of 30 K for the T-$Zr_xHf_{1-x}S_2$ alloy.

3.1.5. Comparison with Previous Modeling Studies. The critical temperatures of the $MS_{2x}Te_{2(1-x)}$ and $MSe_{2x}Te_{2(1-x)}$ alloys with M = Mo or W have been computed before in ref 20, which used a mean field approximation of the configurational entropy and the Perdew−Burke−Ernzerhof exchange−correlation functional. Here, we go beyond a mean field approximation by using MC simulations that explicitly sample the compositional configuration space and use a different exchange−correlation functional that has been shown to provide a good description of these systems.[48] Overall, we find a qualitative agreement, and in the case of the Se−Te alloys, there is a satisfying quantitative agreement as well. We predict that the critical temperature is 270 K (200 K) to be compared with 360 K (280 K) for the W (Mo)-based alloy. For the S−Te alloys, however, we find considerably lower critical temperatures of 370 K (240 K) to be compared with 690 K (490 K) for the W (Mo)-based alloy. If a mean field model for the entropy is used, the critical temperatures for the S−Te alloys increase by 70−80 K. It is also apparent that the present calculations yield a more asymmetric phase diagram, as already noted above. This suggests that the explicit treatment of the configurational entropy and the exchange−correlation are likely to play a role here.

It has been previously estimated based on a mean field approximation of the configurational entropy that the critical temperature for the order−disorder transition in the $Mo_{1-x}W_xS_2$ alloy for $x = 1/3$ and $x = 2/3$ is around 40 K,[23] which is very close to the value of 30 K obtained here.

3.2. Models for Predicting the Alloying Behavior. In the previous sections, we already indicated how certain properties of the boundary phases can serve as qualitative predictors for the properties of the mixed system. Now, we aim to analyze such relations more quantitatively. In the case of a *metallic* (binary) alloy, the Hume-Rothery rules are well-established as a set of basic conditions under which one can expect mixing. According to these (qualitative) rules, mixing ought to be possible if (i) the relative difference of the covalent radii of the components is less than 15% and the components have (ii) similar electronegativity as well as (iii) the same electronic valency. Even though these rules have been formulated for metallic systems, they can still partially explain the mixing behavior in several of the TMD alloys considered here. The Hume-Rothery conditions are, however, based on the properties of the free atoms and as such do not account for any many body interactions in the boundary phases. For example, in the case of MSTe alloys, the covalent radii of the chalcogens exhibit a 30% difference, yet the critical temperature ranges from around 200 K to around 1000 K, indicating that the contributions from interactions in the boundary phases are crucial for the alloying behavior.

It can be a daunting task to identify the features of the boundary phases that are the most suitable for predicting alloying ability. Thankfully, there are machine learning methods that are very well-suited for this task. For this purpose, here, we employ the sure independence screening and sparsifying operator (SISSO) approach that provides an automatized procedure for feature selection to construct predictors for the critical temperature as well as the alloy category (Figure 3).[64] To this end, we considered the following properties of the boundary phases: lattice parameters (a_0), covalent radii, BECs, electronegativities, unit cell areas (A), sheet modulus (B), ionization potential (IP), electron affinity (χ), and work function. Original features were constructed as the magnitude of the difference between the boundary phases. Since we found the sign of the BECs to be relevant in the case of the Janus monolayers (Section 3.1.3) for the categorization model, we constructed the signed BEC features as

$$\gamma_{\mathrm{BEC}} = \frac{\mathrm{Tr}(\mathcal{Z}_1^*) - \mathrm{Tr}(\mathcal{Z}_0^*)}{\mathrm{Tr}(\mathcal{Z}_0^*)} \tag{1}$$

where $\mathrm{Tr}(\mathcal{Z}_1^*) > \mathrm{Tr}(\mathcal{Z}_0^*)$ for the two boundary phases indicated with subscripts 0 and 1, respectively. This quantity provides the information regarding the BECs, removes the ambiguity due to the large anisotropy of the monolayers, and at the same time contains information regarding the sign of the BECs.

We note that some of the considered features are highly correlated, for example, the lattice parameter depends on the character of the bonding in the solid, which is also connected to the BECs, electronegativity, and bulk modulus.

With the exception of only three systems, the critical temperatures of the X-site alloys considered here are below 370 K. We therefore only consider M-site alloys here, for which we seek a linear relationship between the descriptor to be determined and the critical temperature. The descriptor that we find via the SISSO is

$$f = \sqrt{|\delta \mathrm{IP}|}\sqrt[3]{|\delta B||\delta A|^2} \tag{2}$$

which yields a root mean square error (RMSE) of 292 K and a coefficient of determination R^2 of 0.956 (Figure 4). The descriptor is not unique and depends on the features considered in the model as well as the set of alloys considered, as discussed in the original study ref 64. More crucially, it, however, provides clear indications as to which boundary phase features to consider when rationalizing the alloying behavior. Specifically, the descriptor here emphasizes that the ionization potential (or the valence band edge position) as well as the sheet modulus and unit cell area are important parameters.

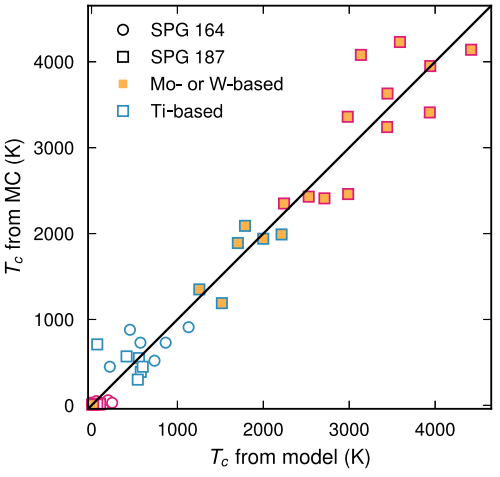

Figure 4. Parity plot of the critical temperature for M-site alloys as computed via MC simulations and the critical temperature model based on the descriptor in eq 2.

https://doi.org/10.1021/acs.chemmater.2c01176
Chem. Mater. XXXX, XXX, XXX−XXX

In addition, we constructed descriptors to enable a categorization of X-site alloys according to the classification introduced in Section 3.1. The resulting model has a 93% success rate in partitioning the different categories of mixing behavior (Figure 5) and uses two descriptors. The first

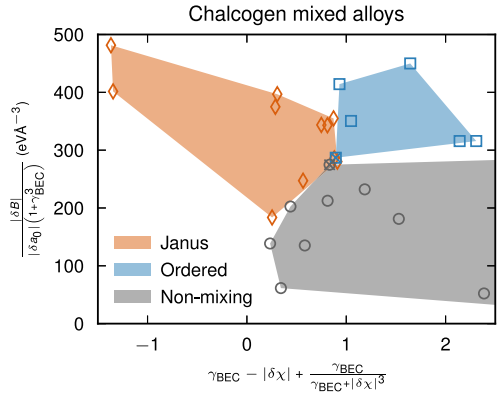

Figure 5. Classification of X-site alloys into ordered, Janus, or non-mixing ground states using the descriptors in eqs 3 and 4.

descriptor (abscissa in Figure 5) obtained via the SISSO is given by

$$d_1 = \gamma_{BEC} - |\delta\chi| + \frac{\gamma_{BEC}}{\gamma_{BEC} + |\delta\chi|^3} \quad (3)$$

It is dimensionless and contains features directly related to bonding (γ_{BEC} and $|\delta\chi|$). The second descriptor (ordinate axis in Figure 5) is

$$d_2 = \frac{|\delta B|}{|\delta a_0|(1 + \gamma_{BEC}^3)} \quad (4)$$

and has units of pressure. Unfortunately, neither of these two descriptors is amenable to a clear physical interpretation.

Two systems are incorrectly categorized. $HfS_{2x}Se_{2(1-x)}$ is categorized as both a Janus system and an ordered system, while in reality, it is an ordered system, yet the Janus structure is only $\lesssim$5 meV f.u.$^{-1}$ compared to other configurations. $PdS_{2x}Se_{2(1-x)}$ (categorized as both non-mixing and Janus) on the other hand is a non-mixing system with a critical temperature of 80 K, but the Janus structure is 30 meV f.u.$^{-1}$ higher in energy than other configurations.

3.3. Electronic Structure. Following the analysis of the thermodynamic properties, we carried out a systematic evaluation of the valence and conduction positions as a function of the composition. From this analysis, we excluded systems with very high critical temperature, leaving us with 48 systems (Figure 6).

To first order, the band edge positions change linearly with composition between the boundary phases, a behavior that is often referred to as Vegard's law. The deviation from this dependence is commonly described by the bowing parameter b, which is defined via

$$\varepsilon(x) = (1 - x)\varepsilon(x = 0) + x\varepsilon(x = 1) - bx(1 - x) \quad (5)$$

where ε represents the concentration-dependent quantity in question. Note that according to this (standard) definition, $-b/4$ corresponds to the deviation from a linear interpolation at $x = 0.5$.

Band edge bowing parameters for $MX_{2x}X'_{2(1-x)}$ for M = Mo and W and X, X′ = S, Se, and Te were already reported in ref 20. The current results are overall in good agreement with these data, albeit slightly smaller in magnitude (Table S5).

The general trend for X-site alloys is that the valence band bowing is negative and increasing in magnitude in the order $S_{2x}Se_{2(1-x)}$, $Se_{2x}Te_{2(1-x)}$, and $S_{2x}Te_{2(1-x)}$ (Figure 6c,d). Especially for the $S_{2x}Te_{2(1-x)}$ alloys, the magnitude of the

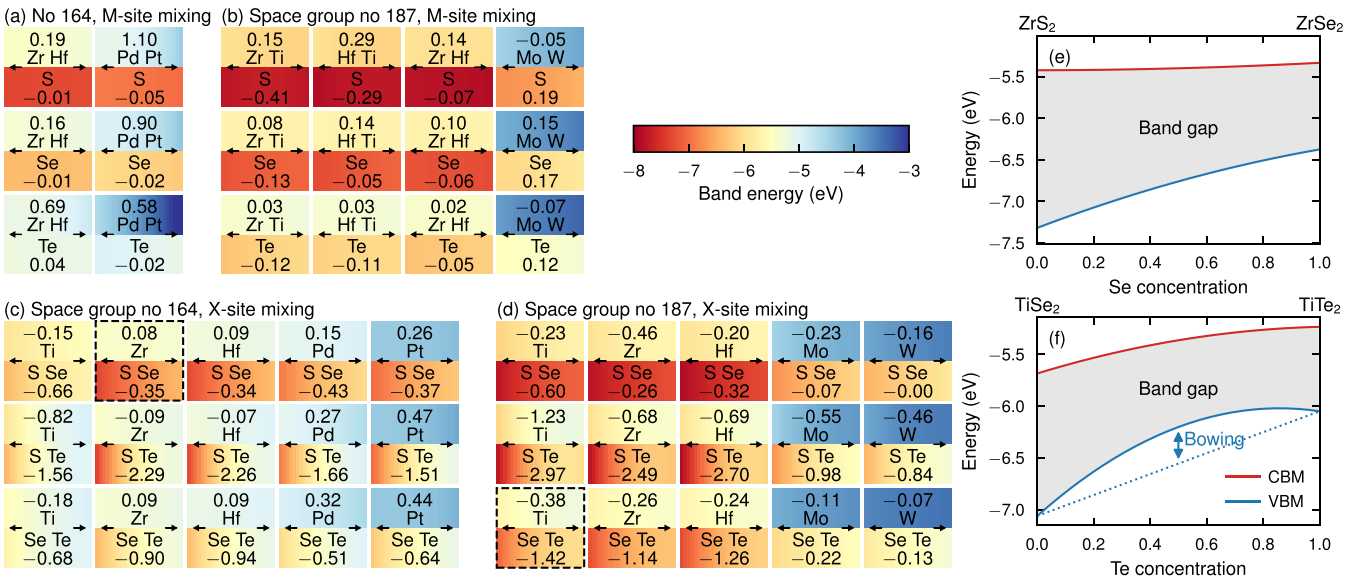

Figure 6. (a–d) Conduction band and valence band edge positions with respect to vacuum for H- and T-type M- and X-site alloys. Each box contains a heat map of the position of the conduction band (top) and valence band (bottom). The bowing parameters (see eq 5) in units of electron volts for the conduction band (valence band) are indicated in the top (bottom) of the box. (e,f) Conduction band minimum (CBM) and valence band maximum (VBM) as a function of the concentration in (e) T-$ZrS_{2(1-x)}Se_{2x}$ and (f) H-$TiSe_{2(1-x)}Te_{2x}$. The bowing parameter is a measure of the deviation of the true band position from a linear interpolation of the band positions of the boundary phases, as indicated by the dotted, blue line in (f).

https://doi.org/10.1021/acs.chemmater.2c01176
Chem. Mater. XXXX, XXX, XXX−XXX

bowing parameter can exceed values of 1 eV. For the conduction band, the variations are generally smaller, and there is no apparent trend that extends through all TMDs. For example, for T-type Zr- and Hf-based TMDs, the bowing parameters for $S_{2x}Se_{2(1-x)}$, $Se_{2x}Te_{2(1-x)}$, and $S_{2x}Te_{2(1-x)}$ are all in the range between 0.07 and 0.09 eV. Furthermore, we find that for X-site alloys, the bowing parameter of the valence band is always negative and that for H-type X-site alloys, the conduction band bowing parameter is always negative. For T-type X-site alloys, the conduction band bowing parameter can have either sign. For example, in T-$HfS_{2x}Se_{2(1-x)}$, the valence band exhibits a bowing parameter of −0.34 eV, while the conduction band bowing parameter is 0.09 eV.

For T-type M-site alloys, the magnitude of the bowing of the valence band edge is generally small, with the maximal (absolute) value of −0.05 eV occurring in T-$Pd_xPt_{1-x}S_2$ (Figure 6a,b). The conduction band edge exhibits significantly larger bowing in this class of alloys with values up to 1.10 eV (in T-$Pd_xPt_{1-x}S_2$). Finally, for H-type M-site alloys, the valence band bowing is larger in magnitude than for T-type M-site alloys with a maximal magnitude of −0.41 eV found in H-$Ti_xZr_{1-x}S_2$. The largest bowing of the conduction band for the H-type M-site alloys is found in $Ti_xHf_{1-x}S_2$ with a value of 0.29 eV.

The valence band and conduction band variations that are possible in the considered alloys are illustrated in Figure 6. Specifically, we find that the variation of the valence band can be very large in $MS_{2x}Te_{2(1-x)}$, for example, in $HfS_{2x}Te_{2(1-x)}$, the difference between the boundary phases is 1.7 eV. In general, the valence band position increases in the series S−Se−Te. The typical behavior is illustrated for T-$ZrS_{2x}Se_{2(1-x)}$ (Figure 6e) and H-$TiSe_{2x}Te_{2(1-x)}$ (Figure 6f).

It has been noted before that the magnitude of the valence band bowing parameter increases in the order $S_{2x}Se_{2(1-x)}$, $Se_{2x}Te_{2(1-x)}$, and $S_{2x}Te_{2(1-x)}$ for H-type Mo- and W-based X-site alloys.[20] Our results show that this trend also holds true for Ti-, Hf-, and Zr-based alloys that exhibit H symmetry and Zr, Hf, Ti, Pd, and Pt alloys that exhibit T symmetry. The band edges exhibit in most cases moderate bowing with the exception of the X-site alloys $MS_{2x}Te_{2(1-x)}$. These are the X-site mixed systems that exhibit the largest lattice constant mismatch and the largest differences in boundary phase features. Therefore, these alloys exhibit the largest variability of the considered alloys. The large bowing parameter in these compounds may however complicate band edge tuning since a small variation in composition is associated with a relatively large variation in the band edge position.

4. CONCLUSIONS

In this study, we have provided a comprehensive study of the phase diagrams and electronic structure of monolayer TMD alloys. It has been shown that mixing systems with in-plane order are absent at room temperature but that specifically, the Ti-based X-site alloys may exhibit a Janus ground state that remains the most stable structure far above room temperature. Furthermore, we have shown that M-site alloys with transition metals from different groups in the periodic table are associated with very high critical temperatures (>1000 K), due to which it is unlikely or at least very difficult for them to be manufactured. The band edges exhibit in most cases little bowing with the exception of X-site alloys that include both S and Te, implying that in many systems, the band edge positions are relatively well-approximated by a linear interpolation of the values of the boundary phases.

■ ASSOCIATED CONTENT

Supporting Information

The Supporting Information is available free of charge at https://pubs.acs.org/doi/10.1021/acs.chemmater.2c01176.

Reference calculations for cluster expansion construction, cluster expansion construction, calculation of critical temperature and order parameters, electronic structure calculations, cluster expansion parameters, boundary phase features, elemental properties, bowing parameters, critical temperatures, valence band edge position of $HfS_{2x}Se_{2(1-x)}$, lattice constants as a function of concentration, mixing energies, and Mc sampling results (PDF)

■ AUTHOR INFORMATION

Corresponding Author

Paul Erhart − *Department of Physics, Chalmers University of Technology, SE-41296 Gothenburg, Sweden;* orcid.org/0000-0002-2516-6061; Email: erhart@chalmers.se

Authors

Christopher Linderälv − *Department of Physics, Chalmers University of Technology, SE-41296 Gothenburg, Sweden*

J. Magnus Rahm − *Department of Physics, Chalmers University of Technology, SE-41296 Gothenburg, Sweden;* orcid.org/0000-0002-6777-0371

Complete contact information is available at: https://pubs.acs.org/10.1021/acs.chemmater.2c01176

Notes

The authors declare no competing financial interest.

■ ACKNOWLEDGMENTS

Funding from the Knut and Alice Wallenberg Foundation (2014.0226 and 2019.0140) as well as the Swedish Research Council (2018-06482 and 2020-04935) is gratefully acknowledged. The computations were enabled by resources provided by the Swedish National Infrastructure for Computing (SNIC) at NSC, C3SE, and HPC2N partially funded by the Swedish Research Council through grant agreement no. 2018-05973.

■ REFERENCES

(1) Mak, K. F.; Lee, C.; Hone, J.; Shan, J.; Heinz, T. F. Atomically Thin MoS_2: A New Direct-Gap Semiconductor. *Phys. Rev. Lett.* **2010**, *105*, 136805.

(2) Andersen, K.; Latini, S.; Thygesen, K. S. Dielectric Genome of van der Waals Heterostructures. *Nano Lett.* **2015**, *15*, 4616−4621.

(3) Naik, M. H.; Jain, M. Ultraflatbands and Shear Solitons in Moiré Patterns of Twisted Bilayer Transition Metal Dichalcogenides. *Phys. Rev. Lett.* **2018**, *121*, 266401.

(4) Brem, S.; Linderälv, C.; Erhart, P.; Malic, E. Tunable Phases of Moiré Excitons in van der Waals Heterostructures. *Nano Lett.* **2020**, *20*, 8534−8540.

(5) Hinnemann, B.; Moses, P. G.; Bonde, J.; Jørgensen, K. P.; Nielsen, J. H.; Horch, S.; Chorkendorff, I.; Nørskov, J. K. Biomimetic Hydrogen Evolution: MoS_2 Nanoparticles as Catalyst for Hydrogen Evolution. *J. Am. Chem. Soc.* **2005**, *127*, 5308−5309.

(6) Yoon, Y.; Ganapathi, K.; Salahuddin, S. How Good Can Monolayer MoS_2 Transistors Be? *Nano Lett.* **2011**, *11*, 3768−3773.

(7) Radisavljevic, B.; Radenovic, A.; Brivio, J.; Giacometti, V.; Kis, A. Single-layer MoS_2 transistors. *Nat. Nanotechnol.* **2011**, *6*, 147−150.

(8) Yao, J.; Yang, G. 2D Layered Material Alloys: Synthesis and Application in Electronic and Optoelectronic Devices. *Adv. Sci.* **2022**, *9*, 2103036.
(9) Mleczko, M. J.; Zhang, C.; Lee, H. R.; Kuo, H.-H.; Magyari-Köpe, B.; Moore, R. G.; Shen, Z.-X.; Fisher, I. R.; Nishi, Y.; Pop, E. $HfSe_2$ and $ZrSe_2$: Two-dimensional semiconductors with native high-κ oxides. *Sci. Adv.* **2017**, *3*, No. e1700481.
(10) Wang, J.; Li, Z.; Chen, H.; Deng, G.; Niu, X. Recent Advances in 2D Lateral Heterostructures. *Nano-Micro Lett.* **2019**, *11*, 48.
(11) Tang, Q.; Jiang, D.-e. Stabilization and Band-Gap Tuning of the 1T-MoS_2 Monolayer by Covalent Functionalization. *Chem. Mater.* **2015**, *27*, 3743−3748.
(12) Raja, A.; et al. Coulomb engineering of the bandgap and excitons in two-dimensional materials. *Nat. Commun.* **2017**, *8*, 15251.
(13) Padilha, J. E.; Peelaers, H.; Janotti, A.; Van de Walle, C. G. Nature and evolution of the band-edge states in MoS_2: From monolayer to bulk. *Phys. Rev. B: Condens. Matter Mater. Phys.* **2014**, *90*, 205420.
(14) Riis-Jensen, A. C.; Manti, S.; Thygesen, K. S. Engineering Atomically Sharp Potential Steps and Band Alignment at Solid Interfaces using 2D Janus Layers. *J. Phys. Chem. C* **2020**, *124*, 9572−9580.
(15) Zhang, C.; Li, M.-Y.; Tersoff, J.; Han, Y.; Su, Y.; Li, L.-J.; Muller, D. A.; Shih, C.-K. Strain distributions and their influence on electronic structures of WSe_2−MoS_2 laterally strained heterojunctions. *Nat. Nanotechnol.* **2018**, *13*, 152−158.
(16) Conley, H. J.; Wang, B.; Ziegler, J. I.; Haglund, R. F.; Pantelides, S. T.; Bolotin, K. I. Bandgap Engineering of Strained Monolayer and Bilayer MoS_2. *Nano Lett.* **2013**, *13*, 3626−3630.
(17) Chen, Y.; Xi, J.; Dumcenco, D. O.; Liu, Z.; Suenaga, K.; Wang, D.; Shuai, Z.; Huang, Y.-S.; Xie, L. Tunable Band Gap Photoluminescence from Atomically Thin Transition-Metal Dichalcogenide Alloys. *ACS Nano* **2013**, *7*, 4610−4616.
(18) Komsa, H.-P.; Krasheninnikov, A. V. Two-Dimensional Transition Metal Dichalcogenide Alloys: Stability and Electronic Properties. *J. Phys. Chem. Lett.* **2012**, *3*, 3652−3656.
(19) Xie, L. M. Two-dimensional transition metal dichalcogenide alloys: Preparation, characterization and applications. *Nanoscale* **2015**, *7*, 18392−18401.
(20) Kang, J.; Tongay, S.; Li, J.; Wu, J. Monolayer semiconducting transition metal dichalcogenide alloys: Stability and band bowing. *J. Appl. Phys.* **2013**, *113*, 143703.
(21) Kutana, A.; Penev, E. S.; Yakobson, B. I. Engineering electronic properties of layered transition-metal dichalcogenide compounds through alloying. *Nanoscale* **2014**, *6*, 5820−5825.
(22) Yang, J.-H.; Yakobson, B. I. Unusual Negative Formation Enthalpies and Atomic Ordering in Isovalent Alloys of Transition Metal Dichalcogenide Monolayers. *Chem. Mater.* **2018**, *30*, 1547−1555.
(23) Tan, W.; Wei, Z.; Liu, X.; Liu, J.; Fang, X.; Fang, D.; Wang, X.; Wang, D.; Tang, J.; Fan, X. Ordered and Disordered Phases in $Mo_{1-x}W_xS_2$ Monolayer. *Sci. Rep.* **2017**, *7*, 15124.
(24) Duan, X.; Wang, C.; Fan, Z.; Hao, G.; Kou, L.; Halim, U.; Li, H.; Wu, X.; Wang, Y.; Jiang, J.; Pan, A.; Huang, Y.; Yu, R.; Duan, X. Synthesis of $WS_{2x}Se_{2-2x}$ Alloy Nanosheets with Composition-Tunable Electronic Properties. *Nano Lett.* **2016**, *16*, 264−269.
(25) Wang, D.; Liu, L.; Basu, N.; Zhuang, H. L. High-Throughput Computational Characterization of 2D Compositionally Complex Transition-Metal Chalcogenide Alloys. *Adv. Theory Simul.* **2020**, *3*, 2000195.
(26) Dumcenco, D. O.; Kobayashi, H.; Liu, Z.; Huang, Y.-S.; Suenaga, K. Visualization and quantification of transition metal atomic mixing in $Mo_{1-x}W_xS_2$ single layers. *Nat. Commun.* **2013**, *4*, 1351.
(27) Xia, X.; Loh, S. M.; Viner, J.; Teutsch, N. C.; Graham, A. J.; Kandyba, V.; Barinov, A.; Sanchez, A. M.; Smith, D. C.; Hine, N. D. M.; Wilson, N. R. Atomic and electronic structure of two-dimensional $Mo_{1-x}W_xS_2$ alloys. *J. Phys. Mater.* **2021**, *4*, 025004.
(28) Apte, A.; Krishnamoorthy, A.; Hachtel, J. A.; Susarla, S.; Idrobo, J. C.; Nakano, A.; Kalia, R. K.; Vashishta, P.; Tiwary, C. S.; Ajayan, P. M. Telluride-Based Atomically Thin Layers of Ternary Two-Dimensional Transition Metal Dichalcogenide Alloys. *Chem. Mater.* **2018**, *30*, 7262−7268.
(29) Tedstone, A. A.; Lewis, D. J.; O'Brien, P. Synthesis, Properties, and Applications of Transition Metal-Doped Layered Transition Metal Dichalcogenides. *Chem. Mater.* **2016**, *28*, 1965−1974.
(30) Zhang, M.; Zhu, Y.; Wang, X.; Feng, Q.; Qiao, S.; Wen, W.; Chen, Y.; Cui, M.; Zhang, J.; Cai, C.; Xie, L. Controlled Synthesis of ZrS_2 Monolayer and Few Layers on Hexagonal Boron Nitride. *J. Am. Chem. Soc.* **2015**, *137*, 7051−7054.
(31) Zhao, Y.; Qiao, J.; Yu, P.; Hu, Z.; Lin, Z.; Lau, S. P.; Liu, Z.; Ji, W.; Chai, Y. Extraordinarily Strong Interlayer Interaction in 2D Layered PtS_2. *Adv. Mater.* **2016**, *28*, 2399−2407.
(32) Haastrup, S.; Strange, M.; Pandey, M.; Deilmann, T.; Schmidt, P. S.; Hinsche, N. F.; Gjerding, M. N.; Torelli, D.; Larsen, P. M.; Riis-Jensen, A. C.; Gath, J.; Jacobsen, K. W.; Jørgen Mortensen, J.-J.; Olsen, T.; Thygesen, K. S. The Computational 2D Materials Database: High-throughput modeling and discovery of atomically thin crystals. *2D Mater.* **2018**, *5*, 042002.
(33) Gjerding, M. N.; et al. Recent progress of the computational 2D materials database (C2DB). *2D Mater.* **2021**, *8*, 044002.
(34) Lau, K. W.; Cocchi, C.; Draxl, C. Electronic and optical excitations of two-dimensional ZrS_2 and HfS_2 and their heterostructure. *Phys. Rev. Mater.* **2019**, *3*, 074001.
(35) Oliver, S. M.; Fox, J. J.; Hashemi, A.; Singh, A.; Cavalero, R. L.; Yee, S.; Snyder, D. W.; Jaramillo, R.; Komsa, H.-P.; Vora, P. M. Phonons and excitons in $ZrSe_2$−ZrS_2 alloys. *J. Mater. Chem. C* **2020**, *8*, 5732−5743.
(36) Gaiser, C.; Zandt, T.; Krapf, A.; Serverin, R.; Janowitz, C.; Manzke, R. Band-gap engineering with HfS_xSe_{2-x}. *Phys. Rev. B: Condens. Matter Mater. Phys.* **2004**, *69*, 075205.
(37) Moustafa, M.; Zandt, T.; Janowitz, C.; Manzke, R. Growth and band gap determination of the ZrS_xSe_{2-x} single crystal series. *Phys. Rev. B: Condens. Matter Mater. Phys.* **2009**, *80*, 035206.
(38) Zhang, J.; Jia, S.; Kholmanov, I.; Dong, L.; Er, D.; Chen, W.; Guo, H.; Jin, Z.; Shenoy, V. B.; Shi, L.; Lou, J. Janus Monolayer Transition-Metal Dichalcogenides. *ACS Nano* **2017**, *11*, 8192−8198.
(39) Riis-Jensen, A. C.; Deilmann, T.; Olsen, T.; Thygesen, K. S. Classifying the Electronic and Optical Properties of Janus Monolayers. *ACS Nano* **2019**, *13*, 13354−13364.
(40) Lu, A.-Y.; et al. Janus monolayers of transition metal dichalcogenides. *Nat. Nanotechnol.* **2017**, *12*, 744−749.
(41) Ångqvist, M.; Muñoz, W. A.; Rahm, J. M.; Fransson, E.; Durniak, C.; Rozyczko, P.; Rod, T. H.; Erhart, P. icet − A Python Library for Constructing and Sampling Alloy Cluster Expansions. *Adv. Theory Simul.* **2019**, *2*, 1900015.
(42) Pedregosa, F.; et al. Scikit-learn: Machine Learning in Python. *J. Mach. Learn. Res.* **2011**, *12*, 2825−2830.
(43) Blöchl, P. E. Projector augmented-wave method. *Phys. Rev. B: Condens. Matter Mater. Phys.* **1994**, *50*, 17953−17979.
(44) Kresse, G.; Hafner, J. Ab initio molecular dynamics for liquid metals. *Phys. Rev. B: Condens. Matter Mater. Phys.* **1993**, *47*, 558−561.
(45) Kresse, G.; Furthmüller, J. Efficiency of ab-initio total energy calculations for metals and semiconductors using a plane-wave basis set. *Comput. Mater. Sci.* **1996**, *6*, 15−50.
(46) Dion, M.; Rydberg, H.; Schröder, E.; Langreth, D. C.; Lundqvist, B. I. Van der Waals Density Functional for General Geometries. *Phys. Rev. Lett.* **2004**, *92*, 246401.
(47) Klimeš, J.; Bowler, D. R.; Michaelides, A. Van der Waals density functionals applied to solids. *Phys. Rev. B: Condens. Matter Mater. Phys.* **2011**, *83*, 195131.
(48) Lindroth, D. O.; Erhart, P. Thermal transport in van der Waals solids from first-principles calculations. *Phys. Rev. B* **2016**, *94*, 115205.
(49) Hart, G. L. W.; Forcade, R. W. Algorithm for generating derivative structures. *Phys. Rev. B: Condens. Matter Mater. Phys.* **2008**, *77*, 224115.

https://doi.org/10.1021/acs.chemmater.2c01176
Chem. Mater. XXXX, XXX, XXX−XXX

(50) Cowley, J. M. X-ray measurement of order in single crystals of Cu_3Au. *J. Appl. Phys.* **1950**, *21*, 24−30.
(51) Zunger, A.; Wei, S.-H.; Ferreira, L. G.; Bernard, J. E. Special quasirandom structures. *Phys. Rev. Lett.* **1990**, *65*, 353.
(52) van de Walle, A.; Tiwary, P.; de Jong, M.; Olmsted, D. L.; Asta, M.; Dick, A.; Shin, D.; Wang, Y.; Chen, L.-Q.; Liu, Z.-K. Efficient stochastic generation of special quasirandom structures. *Calphad* **2013**, *42*, 13.
(53) Berland, K.; Hyldgaard, P. Exchange functional that tests the robustness of the plasmon description of the van der Waals density functional. *Phys. Rev. B: Condens. Matter Mater. Phys.* **2014**, *89*, 035412.
(54) Heyd, J.; Scuseria, G. E.; Ernzerhof, M. Hybrid functionals based on a screened Coulomb potential. *J. Chem. Phys.* **2003**, *118*, 8207−8215 erratum: ibid. 124, 219906 (2006).
(55) Heyd, J.; Scuseria, G. E.; Ernzerhof, M. Erratum: ″Hybrid functionals based on a screened Coulomb potential″ [J. Chem. Phys. 118, 8207 (2003)]. *J. Chem. Phys.* **2006**, *124*, 219906.
(56) Hume-Rothery, W.; Mabbott, W.; Gilbert; Channel Evans, K. M.; Carpenter, H. C. H. The freezing points, melting points, and solid solubility limits of the alloys of silver and copper with the elements of the B sub-groups. *Philos. Trans. R. Soc., A* **1934**, *233*, 1−97.
(57) Allred, A. L. Electronegativity values from thermochemical data. *J. Inorg. Nucl. Chem.* **1961**, *17*, 215−221.
(58) Pike, N. A.; Van Troeye, B.; Dewandre, A.; Petretto, G.; Gonze, X.; Rignanese, G.-M.; Verstraete, M. J. Origin of the counterintuitive dynamic charge in the transition metal dichalcogenides. *Phys. Rev. B* **2017**, *95*, 201106.
(59) Hibino, Y.; Yamazaki, K.; Hashimoto, Y.; Oyanagi, Y.; Sawamoto, N.; Machida, H.; Ishikawa, M.; Sudo, H.; Wakabayashi, H.; Ogura, A. The Physical and Chemical Properties of $MoS_{2(1-x)}Te_{2x}$ Alloy Synthesized by Co-sputtering and Chalcogenization and Their Dependence on Fabrication Conditions. *MRS Adv.* **2020**, *5*, 1635−1642.
(60) Susarla, S.; Kochat, V.; Kutana, A.; Hachtel, J. A.; Idrobo, J. C.; Vajtai, R.; Yakobson, B. I.; Tiwary, C. S.; Ajayan, P. M. Phase Segregation Behavior of Two-Dimensional Transition Metal Dichalcogenide Binary Alloys Induced by Dissimilar Substitution. *Chem. Mater.* **2017**, *29*, 7431−7439.
(61) Sahoo, P. K.; Memaran, S.; Xin, Y.; Balicas, L.; Gutiérrez, H. R. One-pot growth of two-dimensional lateral heterostructures via sequential edge-epitaxy. *Nature* **2018**, *553*, 63−67.
(62) Susarla, S.; Hachtel, J. A.; Yang, X.; Kutana, A.; Apte, A.; Jin, Z.; Vajtai, R.; Idrobo, J. C.; Lou, J.; Yakobson, B. I.; Tiwary, C. S.; Ajayan, P. M. Thermally Induced 2D Alloy-Heterostructure Transformation in Quaternary Alloys. *Adv. Mater.* **2018**, *30*, 1804218.
(63) Yuan, J.; Yu, N.; Wang, J.; Xue, K.-H.; Miao, X. Design lateral heterostructure of monolayer ZrS_2 and HfS_2 from first principles calculations. *Appl. Surf. Sci.* **2018**, *436*, 919−926.
(64) Ouyang, R.; Curtarolo, S.; Ahmetcik, E.; Scheffler, M.; Ghiringhelli, L. M. SISSO: A compressed-sensing method for identifying the best low-dimensional descriptor in an immensity of offered candidates. *Phys. Rev. Mater.* **2018**, *2*, 083802.

https://doi.org/10.1021/acs.chemmater.2c01176
Chem. Mater. XXXX, XXX, XXX−XXX